ACS Energy LETTERS

http://pubs.acs.org/journal/aelccp

Activation Energy Assessing Potential-Dependent Activities and Site Reconstruction for Oxygen Evolution

Tilahun Awoke Zegeye, Wen-Tai Chen, Chun-Cheng Hsu, Joey Andrew A. Valinton, and Chun-Hu Chen*

Cite This: *ACS Energy Lett.* 2022, 7, 2236–2243

Read Online

ACCESS | Metrics & More | Article Recommendations | Supporting Information

ABSTRACT: We demonstrated the activation energy approach to evaluate oxygen evolution performance and to probe active site reconstruction at different potentials. Activation energies are acquired following the Arrhenius equation by monitoring the current densities under varied hydroxide concentrations and temperatures. Our complex oxide electrocatalysts (Ag- and Ce-bidoped iron manganese oxyhydroxide) exhibit a much smaller activation energy of 19.12 kJ mol^{-1} in comparison to FeMnOH (60.01 kJ mol^{-1}) at 1.7 V. The higher numbers of doped metal cations show smaller activation energy values corresponding to the higher activities, yet site reconstruction is less likely to occur. Through *operando* Raman studies, site reconstruction may not be absolutely required to reach a high-performance OER, in contrast to the general recognition. By knowing the potential-dependent activation energy, a quantitative OER activity comparison among reconstructed sites is possible. A substrate with a low background current is useful to experimentally acquire *iR*-corrected activation energies over a wide potential window.

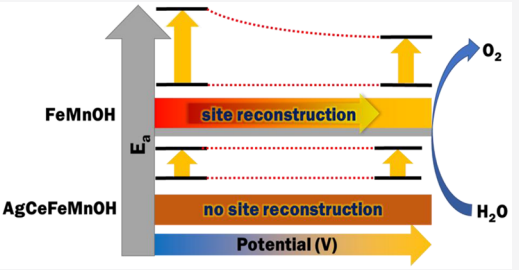

Reconstruction of active sites usually occurs in the alkaline electrocatalytic oxygen evolution reaction (OER).[1−6] Typical examples are transition-metal oxides of cobalt, iron, and nickel transforming into the corresponding amorphous oxyhydroxides (CoOOH, FeOOH, and NiOOH) at elevated potentials, which are intrinsically much more active than the preactivated form of oxides.[7−9] Knowledge of detecting and understanding the actual configurations of these rearranged sites is, of course, critical to realize smarter designs of future OER electrocatalysts, but it is also challenging. Studies show that these reconstructions rapidly turn back to the preactivated forms as soon as the bias potential is removed,[10] resulting in an even more difficult situation to resolve reconstructed sites in a potential-dependent manner. Detailed information on such a potential-dependent reconstruction needs simple, effective experimental approaches to monitor, since the recent advancement of designs has been toward doping high numbers (>3) of different dopants in one electrocatalyst.[2,11]

To recognize the occurrence of potential-dependent reconstruction, *operando* characterization techniques (such as X-ray, Raman, FTIR, etc.)[10,12,13] are needed, but they are not easy to accomplish since skillful operation and expensive instruments are required. The most common index of OER activity in the literature is probably the overpotential, which is a potential gap on top of the thermodynamic minimum of 1.23 V to drive the OER at a certain current density (usually 10 mA cm^{-2}).[14,15] Although the overpotential is useful to evaluate the overall performance from an engineering aspect (e.g., device or cell rack construction), intrinsic and extrinsic factors, such as site reconstruction and changes in electrochemical surface areas, cannot be truly appreciated or distinguished. Some bumpy features in linear sweep voltammetry (LSV) curves (e.g., $Ni^{II/III}$ and $Co^{II/III}$ transition) serve as an index of recognizing surface reconstruction.[16−18] Yet this scenario would not be effective enough when there are multiple reconstruction stages. Tafel slopes are mainly used to present the ratios between the applied potential and the increased OER current, providing little information regarding reconstruction behaviors. Until now, *operando* techniques are still the only, most trustworthy choices for a deep inspection of electrocatalyst reconstruction, even though the accessibility is quite low among most of the research institutes/groups.

Received: May 11, 2022
Accepted: June 2, 2022

https://doi.org/10.1021/acsenergylett.2c01103
ACS Energy Lett. 2022, 7, 2236−2243

Table 1. Comparison of Activation Energy Differences among the Complex Oxide Catalysts, together with Their Electrochemical Surface Areas and Mole Ratios before and after the OER

	activation energy (E_a) at FTO (kJ mol^{-1})			electrochemical surface area (ECSA)			mole ratio (ICP-based)		
catalysts	1.7 V	2.0 V	ΔE_a[a]	pre-OER	post-OER	change (%)[b]	precursor	synthesized	after OER
FeMnOH	60.01	34.26	25.75	3.25	3.35	3.08	3:1[c]	2.89:1[c]	1.72:1[c]
AgFeMnOH	42.96	19.87	23.09	3.80	3.91	2.89	0.3:2.7:1[d]	0.37:2.65:1[d]	0.03:2.83:1[d]
CeFeMnOH	36.35	16.74	19.61	4.29	4.20	2.09	0.3:2.7:1[e]	0.3:2.73:1[e]	0.33:2.87:1[e]
AgCeFeMnOH	19.12	13.99	5.13	4.25	4.21	0.09	0.09:0.23:2.98:1[f]	0.062:0.22:2.97:1[f]	0.064:0.21:2.95:1[f]

[a]Difference between E_a values at 1.7−2.0 V. [b]Change (%) = $|ECSA_{post\text{-}OER} - ECSA_{pre\text{-}OER}|/ECSA_{Pre\text{-}OER} \times 100\%$. [c]Ratio corresponding to the elemental Fe:Mn mole ratio. [d]Ratio corresponding to the elemental Ag:Fe:Mn mole ratio. [e]Ratio corresponding to the elemental Ce:Fe:Mn mole ratio. [f]Ratio corresponding to the elemental Ag:Ce:Fe:Mn mole ratio.

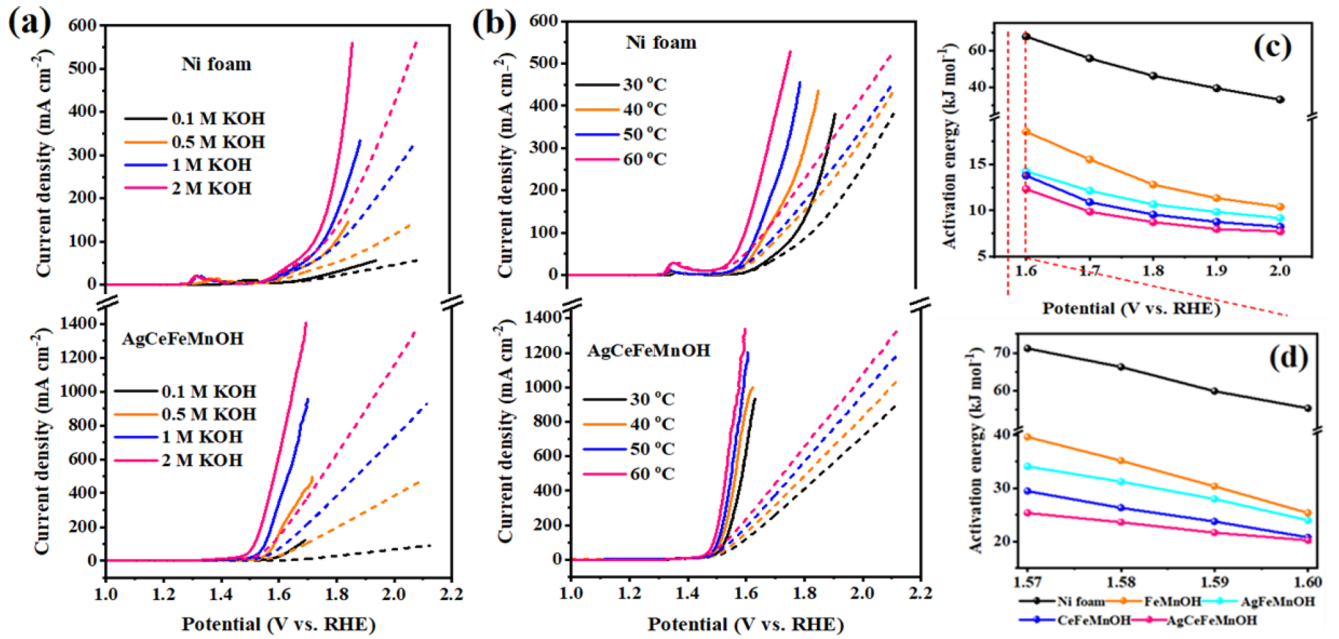

Figure 1. Electrochemical results toward measuring the activation energy of the complex oxide electrocatalysts. (a) Electrolyte-concentration-dependent polarization curves of Ni foam and AgCeFeMnOH to determine the catalytic reaction order. (b) Temperature-dependent polarization curves of Ni foam and AgCeFeMnOH. All iron-free samples were recorded in iron-free 1 M KOH at 50 mV s^{-1}. The solid and dashed lines in (a) and (b) represent the data measured with and without *iR* correction, respectively. Comparison of OER activation energies (E_a) of the Ni foam and all of the complex oxide samples at different operating potentials (c) without and (d) with *iR* corrections, respectively. The potential window to monitor the *iR* corrected activation energy evaluation of (d) becomes very small (1.57−1.60 V), corresponding to the region between the red dashed lines indicated in (c).

The activation energy of a catalyst is known to highly depend on the local configurations of active sites and thus should be a suitable index to probe the occurrence of active site reconstruction. By measuring the activation energy along varied potentials, one could quantitatively draw profiles of the potential-dependent reconstruction of electrocatalysts.

Here, we propose and report the successful exploration of obtaining the alkaline OER activation energy (E_a from the Arrhenius equation) to evaluate electrocatalytic performance and acknowledge the occurrence of active site reconstruction. The benchmark of Ni foam indeed shows potential-dependent reconstruction by a combination of simple LSV measurements under different electrolyte concentrations and temperatures. Upon testing the iron manganese based oxide electrocatalysts, a key discovery is that the higher dopant numbers significantly inhibit site reconstruction yet enhance the OER activities. The optimal performance of the complex oxides in our case (i.e., Ag- and Ce-bidoped FeMn oxyhydroxide) highlight that reconstruction is not always needed to realize the ultimate reactivity, suggesting a new, practical angle of using the activation energy to revisit active sites of complex oxide electrocatalysts.

A single-step acidic redox-assisted deposition (ARD) process in our previous works was used to synthesize all of the complex multinary metal oxide electrocatalysts on Ni foam (see the Supporting Information).[13,16,19,20] The redox between $FeSO_4$ and $KMnO_4$ was the driving force to yield iron manganese oxyhydroxide (FeMnOH), with a typical ratios of Fe/Mn = 2.89/1 (see Table 1). The two dopants Ag^+ and Ce^{4+} were introduced by adding the precursors $AgNO_3$ and $Ce(NO_3)_3$ to the preparation mixture of FeMnOH. The total doping levels in the preparation procedure were all controlled to be 10 mol % for both Ag-doped FeMnOH (denoted as AgFeMnOH) and Ce-doped FeMnOH (denoted as CeFeMnOH), while the bidoped cases (denoted as AgCeFeMnOH) were synthesized with 3 mol % of Ag and 7 mol % of Ce (a total of 10%) as the optimal samples. Ce was incorporated to create oxygen vacancy defects to favor oxide-material-driven electrocatalysis such as the OER,[21−24] while Ag was added to improve the conductivity

https://doi.org/10.1021/acsenergylett.2c01103
ACS Energy Lett. 2022, 7, 2236−2243

Table 2. Summary of Experimentally Determined Reaction Orders of Different Complex Metal Oxide Electrocatalysts at Different Potentials in the OER

	order of reaction (x)[a]										
	Ni foam substrate (no *iR* correction)				Ni foam substrate (with *iR* correction)			FTO substrate (with *iR* correction)			
catalysts	1.7 V	1.8 V	1.9 V	2.0 V	1.58 V	1.60 V	1.62 V	1.7 V	1.8 V	1.9 V	2.0 V
Ni foam	0.71	0.715	0.70	0.73	0.99	1.02	1.00				
FeMnOH	0.72	0.67	0.65	0.64	1.11	1.05	1.02	0.95	0.97	0.90	0.83
AgFeMnOH	0.88	0.83	0.78	0.78	1.09	0.92	1.06	0.90	0.87	0.80	0.80
CeFeMnOH	0.90	0.84	0.81	0.80	1.19	1.24	1.06	0.94	0.87	0.75	0.69
AgCeFeMnOH	0.801	0.812	0.815	0.815	1.10	1.04	0.98	0.96	0.93	0.84	0.83

[a]Average of all the individual x values obtained by measurement in iron-free KOH under certain conditions (on the basis of the data in Tables S1 and S2).

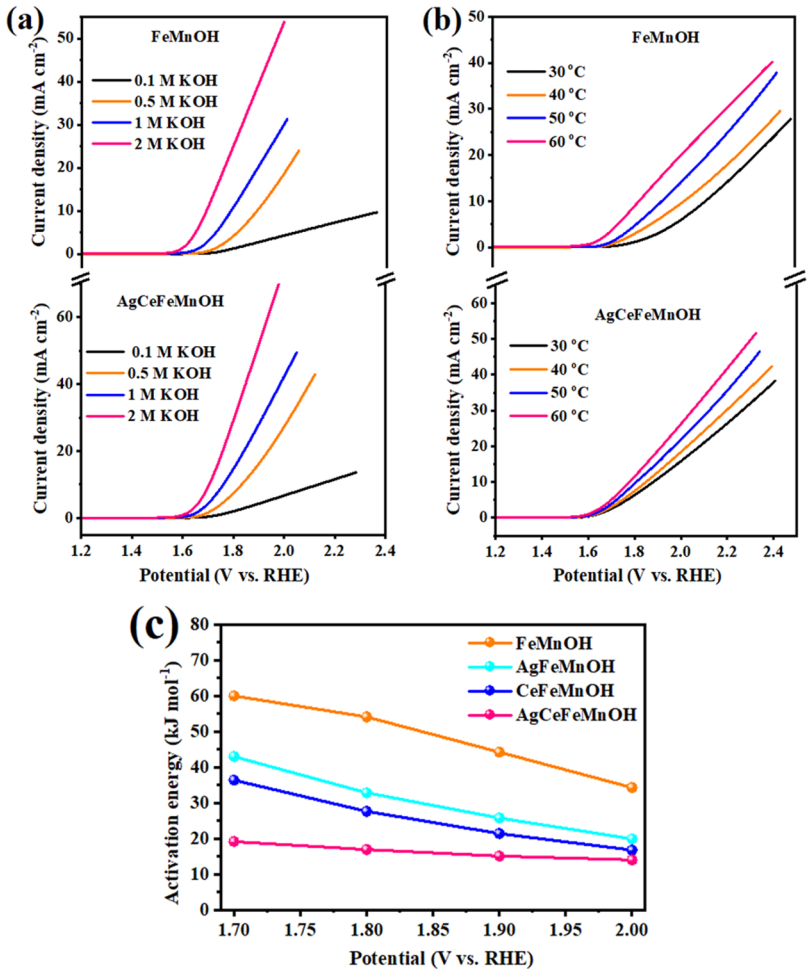

Figure 2. Electrochemical results toward measuring the activation energy of the complex oxide electrocatalysts grown on an FTO substrate with *iR* correction. (a) Electrolyte-concentration-dependent OER polarization curves of FeMnOH and AgCeFeMnOH and (b) the temperature-dependent curves recorded in 1 M KOH at 50 mV s^{-1}. (c) Comparison of OER activation energies of all the complex oxides at different potentials.

toward an enhanced OER performance.[25] The ICP data (Table 1) confirm the presence of the corresponding dopants in the samples. The TEM characterization shows that all of the pristine and doped FeMnOH samples are deposited as a uniform, amorphous thin coating (30.3 nm thickness) along the surface of the substrates (Figure S1). No complex surface morphology of the coating was observed, suggesting similar geographic surface areas between the samples.

To obtain the activation energy (E_a) with the Arrhenius equation, we need to measure reaction rate constants (k) first. In the alkaline OER, the main reaction is given by eq 1.[26,27]

$$4OH^-(aq) \rightarrow O_2(g) + 2H_2O(l) + 4e^- \quad (1)$$

Thus, the reaction rates can be expressed as oxygen gas production in a unit of time, as a function of hydroxide ion concentration (eq 2).

https://doi.org/10.1021/acsenergylett.2c01103
ACS Energy Lett. 2022, 7, 2236−2243

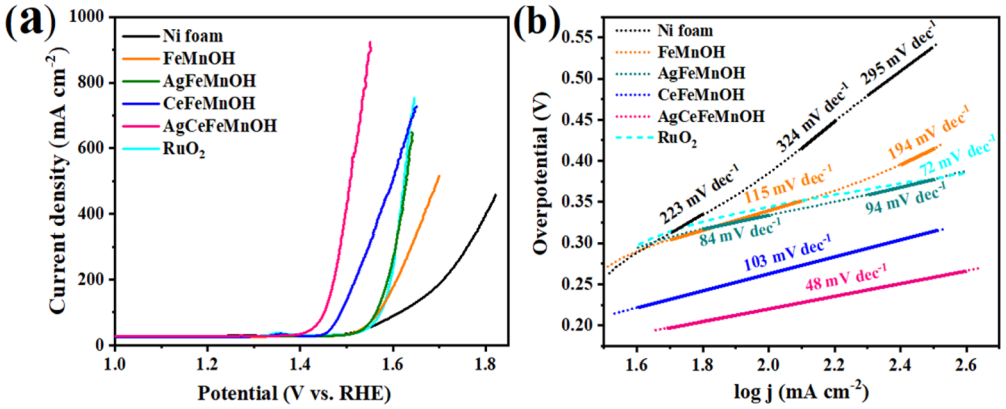

Figure 3. OER electrochemical performance of Ni foam, RuO_2, and all of the complex oxide samples on Ni foam. (a) Polarization curves at room temperature under 1 M KOH with a scan rate of 50 mV s^{-1} and (b) the corresponding Tafel plots.

$$\frac{\Delta[O_2]}{\Delta t} = k[OH^-]^x \quad (2)$$

The production rate of oxygen gas is directly proportional to the quantity of current generated through the number of electron transfers per unit area (eq 3)

$$\frac{i}{nFA} = k[OH^-]^x \quad (3)$$

where i/A is the current density obtained from the LSV curve at different applied potentials (V vs. RHE), n is the number of electron transfers during the OER (n = 4), F is the Faraday constant (96485 C mol^{-1}), and x is the order of the catalytic reaction.

To determine the reaction order, we measured the current density of LSV curves of the catalysts, of which Ni foam and AgCeFeMnOH are representative samples (all other catalysts are given in the Supporting Information), with different concentrations of electrolyte (i.e., 0.1, 0.5, 1, and 2 M KOH) with and without iR correction, presented as solid and dashed lines, respectively, in Figure 1a. By plugging data into eq 3, we determined the order of the reaction (x values of eq 3) at different applied potentials as summarized in Table 2. For the non-iR-corrected condition, the available current values for the reaction order measurements are within the potential range of 1.7−2.0 V. In general, the x values remain nearly the same over the potential ranges. Pristine Ni foam shows an average value of x of 0.71, while AgCeFeMnOH on Ni foam gives an average x value of 0.812, which is very close to that of Ni foam.

However, after iR correction, the very steep increase in current density results in a difficult situation that the potential windows available to determine the reaction order become very narrow (i.e., 1.58−1.62 V; see Table 1). This issue is attributed to the high background current using Ni foam as substrate (e.g., >600 mA cm^{-2} at 1.65 V). Such an issue has been reported in previous research,[28] but no experimental approach has been effectively applied to solve it. To overcome this difficulty, we used fluorine-doped tin oxide (FTO) as a low-background-current substrate, rather than Ni foam (the deposition procedures of all the complex oxides on FTO via ARD are given in the Supporting Information). The as-measured LSV results (Figure 2a) show a wide potential window of iR-corrected reaction orders becomes possible (i.e., 1.7−2.0 V vs RHE). This might be the first experimental proof of the direct observation of the trend of iR-corrected reaction orders in a wide potential range, and the trend is similar to that of before the iR correction. These results agree with the reported data by the Lyons and Bell groups,[29,30] where the reaction order was considered to be 1. Thus, the first-order reaction rate law of the alkaline OER independent of the tested potential ranges has been confirmed.

After the determination of reaction order, the rate constants (k) can be obtained at different temperatures (Figures 1b and 2b and Figures S2−S4). According to the Arrhenius equation (eq 4), one can obtain E_a at various potentials[31−35]

$$\ln k = -\frac{E_a}{RT} + \ln A \quad (4)$$

where k is the reaction rate constant, A is the frequency factor, R is the universal gas constant, and T is the absolute temperature (30−60 °C).

The E_a values of bare Ni foam are shown in Figure 1c,d (in the absence and presence of iR correction, respectively), giving a common trend that, by increasing the potentials, the activation energy gradually decreases. At an overpotential of 350 mV (1.58 V vs RHE), our iR-corrected Ni foam has an E_a value of 68 kJ mol^{-1}, which indicates the formation of $Ni(OH)_2$/NiOOH, in line with previously reported values in iron-free KOH at a similar potential (~72 kJ mol^{-1}).[15] This potential-dependent activation energy agrees with the reconstruction process of NiO into γ-NiOOH together with the increased OER reactivity.[31]

On the other hand, the E_a values of all the complex oxides in Figure 1c,d are shown to be smaller than that of Ni foam. As shown in Figure 2c, a general trend is that higher numbers of incorporated cations give lower activation energies in a wide potential range (1.7−2.0 V) with iR correction. A comparison of E_a values (at 2.0 V vs RHE) shows the increasing order AgCeFeMnOH (13.99 kJ mol^{-1}) < CeFeMnOH (16.74 kJ mol^{-1}) ≈ AgFeMnOH (19.87 kJ mol^{-1}) < FeMnOH (34.26 kJ mol^{-1}) on FTO, while the E_a value of blank FTO is 56.47 kJ mol^{-1}. In an attempt to validate our measurements, we compared the E_a of a widely available commercial benchmark (i.e., RuO_2) to the literature value using FTO as an electrode (Figure S4), since E_a values of electrocatalysts are dependent on the substrates. Our tests show that commercial RuO_2 deposited on FTO exhibits an E_a value of 35.95 kJ mol^{-1} at 1.7 V, similar to the reported values (38−42.5 kJ mol^{-1}).[36−38] With these good agreements of values together with the E_a value of Ni foam in an iron-free electrolyte, the accuracy of our measurement can be validated. More importantly, the activation energy of the samples with higher numbers of dopants is less sensitive to an

https://doi.org/10.1021/acsenergylett.2c01103
ACS Energy Lett. 2022, 7, 2236−2243

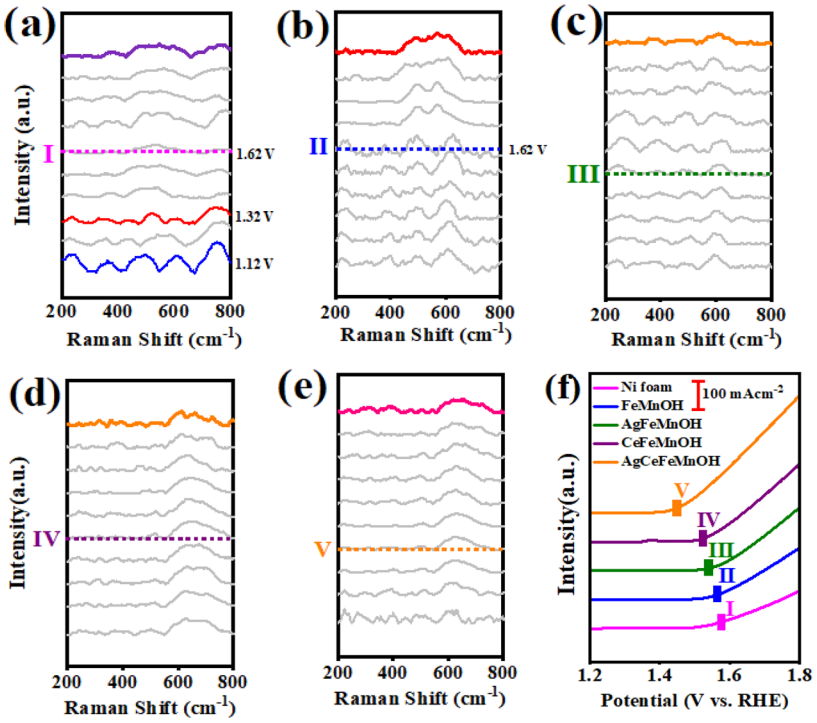

Figure 4. Electrochemical-coupled Raman spectra of the electrocatalysts: (a) Ni foam; (b) FeMnOH; (c) AgFeMnOH; (d) CeFeMnOH; (e) AgCeFeMnOH. Each Raman plot is measured using 1 M KOH under constant chronoamperometric potentials ranging from 1.12 to 2.02 V (vs RHE) with 0.1 V increments at room temperature. Pristine Ni foam and FeMnOH show multiple- and two-stage phase transitions, respectively, while the other samples barely show changes during the OER. (f) *Operando* electrochemical responses. The Roman numeral labels (I–V) indicating each inflection point correspond to the OER onset potentials of the catalysts. These onset potentials are also highlighted as the horizontal dashed lines in the corresponding Raman spectra in (a–e).

increase in the applied potential (Figure 2c). In Table 1, the ΔE_a values between 1.7 and 2.0 V of AgCeFeMnOH and FeMnOH are 5.13 and 25.75 kJ mol^{-1}, respectively, which indicates fewer degrees of site reconstruction with increased numbers of metal cations in the complex oxide samples.

To confirm whether a smaller activation energy indeed corresponds to a higher OER activity, a series of electrochemical tests was carried out, as shown in Figure 3. The LSV results (Figure 3a) show that the performance of AgCeFeMnOH is much greater than that of Ni foam. In a range of 1.57–1.60 V, the increasing order of current density is 67.48–88.8 mA cm^{-2} (Ni foam) < 102.32–176.44 mA cm^{-2} (FeMnOH) < 89.56–233 mA cm^{-2} (RuO_2) < 119.64–262.52 mA cm^{-2} (AgFeMnOH) < 393.88–502 mA cm^{-2} (CeFeMnOH) < 922.5 mA cm^{-2} (AgCeFeMnOH). This sequence clearly supports that a smaller activation energy represents a greater OER reactivity and further recognizes that the higher numbers of incorporated metal cations result in the greater OER current density (AgCeFeMnOH > CeFeMnOH ≈ AgFeMnOH > FeMnOH). The optimal AgCeFeMnOH indeed shows OER activity superior to that of the benchmark RuO_2, as predicted by an activation energy comparison. Accordingly, AgCeFeMnOH should be more active (13–19 kJ mol^{-1}) than NiFeMo (20.32 kJ mol^{-1})[39] and close to the well-reputed IrO_2 (15–16 kJ mol^{-1})[40] in the literature.

A Tafel slope comparison at the initial stage of the OER (Figure 3b) shows the increasing order AgCeFeMnOH (48 mV dec^{-1}) < RuO_2 (72 mV dec^{-1}) < AgFeMnOH (84 mV dec^{-1}) < CeFeMnOH (103 mV dec^{-1}) < FeMnOH (115 mV dec^{-1}) < Ni foam (223 mV dec^{-1}), which shares a common trend with the E_a values above. Since the intercept with the log |j| axis can be extrapolated from the Tafel slope,[41] which is directly proportional to the E_a value,[42,43] a lower Tafel slope should correspond to a lower E_a value, which is in agreement with our electrochemical results. The electrochemical surface area (ECSA), normalized by referencing Ni foam (1.00) in Table S3, shows similar values among samples of AgCeFeMnOH (4.25), FeMnOH (3.25), and RuO_2 (3.14). These small ECSA deviations may not be the major reason for the drastic difference in OER performance among these catalysts (Figure 3a). These correlations clearly justify the effectiveness of using the activation energy to be a comprehensive, useful index of the overall OER performance of the complex oxide electrocatalysts. In addition, these complex oxides intrinsically possess high-activity OER sites that would not require significant reconstruction as Ni foam does to reach further activated configurations.

To further investigate the occurrence of active site reconstruction at various potentials, we conducted an *operando* Raman study (also known as electrochemical-coupled Raman spectroscopy), as shown in Figure 4.[44] Horizontal dashed lines were set on the Raman spectra on each catalyst (labeled as **I–V**) and are defined as the OER onset potentials. These potentials can be defined as that corresponding to the inflection point between the non-Faradaic and the OER-active current[45] in their respective LSV plots (Figure 4f). Hence, the results above the dashed line in each catalyst were measured alongside a potential that activates the OER. At 1.12 V, Ni foam exhibits several broad bands corresponding to mixed vibration signals of NiO (345, cm^{-1}), Ni film (591 cm^{-1}) and α-Ni(OH)$_2$ (450 and 770 cm^{-1})[33,46] (Figure 4a). At 1.32 V, the newly emerging band at 519 cm^{-1}, representing the harmonic overtone belonging to a

https://doi.org/10.1021/acsenergylett.2c01103
ACS Energy Lett. 2022, 7, 2236–2243

vibration at 260 cm^{-1} of β-$Ni(OH)_2$, together with the vanishing of the 770 cm^{-1} band of α-$Ni(OH)_2$, suggests a transformation from α-$Ni(OH)_2$ to β-$Ni(OH)_2$.[47] The onset potential acquired from Figure 4f is indicated by the pink dashed line labeled as **I**, where a broad band (i.e., ranging from 450 to 650 cm^{-1}) arises right beyond the onset potential line, corresponding to NiOOH, and continuously appears up to 2.02 V.[48] To eliminate intense bubbling that might interfere with the Raman measurements at this stage, electrode degassing by bubbling inert gas was carried out (see the Supporting Information). These results confirm a series of active site reconfigurations that directly correlates to the drastic, potential-dependent activation energy as shown in Figures 1c,d and 2c. This also shows that the OER reactivities between each of the evolved sites at various potentials can be therefore quantitatively evaluated.

For FeMnOH (Figure 4b), an appreciable phase change at 1.62 V can be observed, which matches with the indicated onset potential line (blue dashed line labeled **II**). Below the onset potential, the Raman bands at 492 and 610 cm^{-1} agree with the vibration mode of Fe−O strength of Fe_2O_3,[49] while above the onset potential line, the signals correspond well to Mn-doped FeOOH.[50] The site reconstruction procedure of FeMnOH is less complicated than that of Ni foam. For AgFeMnOH (Figure 4c), the spectra below the onset potential line (green dashed line labeled **III**) are very similar to those of FeMnOH, while the selectively enhanced symmetric vibration of Fe−O at 300 cm^{-1} was observed above 1.52 V. In CeFeMnOH (Figure 4d), the additional broad Raman band around 650 cm^{-1} may correspond to γ-FeOOH,[51] and negligible reconstructions over the entire potential range, including these above and below the onset potential line **IV**, have been recognized. For the bidoped AgCeFeMnOH (Figure 4e), the spectra are closer to those of CeFeMnOH than to those of AgFeMnOH with nearly no sign of site reconstruction. All of the data suggest a trend that with higher numbers of doped cations fewer degrees of site reconstruction are likely to occur, which agrees well with the similar trend of ΔE_a in Table 1.

To further inspect the site reconstruction degrees in addition to the *operando* Raman technique, the changes in ECSA, elemental compositions, and surface morphologies of pre- and post-OER have been compared. In terms of ECSA values (Table 1), Ni foam has the highest change in electroactive surface (50.0%), while AgCeFeMnOH yields the least change (0.09%), followed by CeFeMnOH (2.09%), AgFeMnOH (2.89%), and FeMnOH (3.08%). The post-OER elemental analysis by ICP (Table 1) indicates a mole ratio change in FeMnOH (Fe:Mn from 2.89:1 to 1.72:1, changed by 40%), while increasing the number of metal cations can inhibit the composition changes (Table 1). A morphological change in the SEM images after the OER (Figure S5) becomes extensive in Ni foam (Figure S5a,b) and relatively mild in FeMnOH (Figure S5c,d), while AgCeFeMnOH showed an insignificant surface change (Figure S5e,f). These results, confirming that the increased number of metal cations in the complex oxide inhibits the site reconstruction, are supplementary to the conclusive message indicated by the *operando* Raman and E_a study.

Since site reconstruction usually changes the intrinsic activation energy, Tafel plots with multiple slope values may be useful to determine the occurrence of site reconstruction, according to the relationship between Tafel slope and activation energy (as discussed earlier). In Figure 3b, we have seen that three different Tafel slopes (223, 324, and 295 mV dec^{-1}) can be derived from Ni foam, meaning that three different active sites evolved over the measured potential range. This corresponds well to the three stages of site evolutions of Ni foam shown in the *operando* Raman data (i.e., α-$Ni(OH)_2$ to β-$Ni(OH)_2$ to NiOOH). Such a correspondence also matches with the two Tafel slopes from FeMnOH (115 and 194 mV dec^{-1}) and AgFeMnOH (84 and 94 mV dec^{-1}) and the single slopes from CeFeMnOH (103 mV dec^{-1}) and AgCeFeMnOH (48 mV dec^{-1}). These relationships suggest that the presence of multistage Tafel slopes could also be recognized as a supplementary index for judgment of the presence of site reconstruction within electrocatalysts.

Although more detailed studies are needed, the data clearly support that a higher activation energy may be associated with a more complicated, multiple-stage reconstruction. A typical comparison is the activation energy sequence Ni foam > FeMnOH > AgFeMnOH ≈ CeFeMnOH > AgCeFeMnOH, agreeing with the trend of site reconstruction degrees as observed in the *operando* Raman, where Ni foam is the most aggressive catalyst undergoing reconstruction. Rearrangements of atoms/ions and chemical bonds should increase the required activation energy barrier to the onset of the OER. On the other hand, since the constituent dopant cations have different oxidation states and sizes, the presence of increased local lattice oxygen vacancies[5] and various metal−oxygen bond strengths, by an increase in the numbers of dopant species, may prevent local dislocation motion/rearrangement and thus inhibit site reconstruction.[52,53] We also argue that AgCeFeMnOH may also have its own reconstruction forms but requires much greater potentials than have been used in this work to be seen. If so, an even higher OER reactivity of AgCeFeMnOH may be exhibited. The most possible scenario to observe/study that could be high-current water splitting.

As indicated above, several important questions still remain unanswered, regarding the detailed configurations of highly active sties in AgCeFeMnOH and actual mechanisms for the inhibited site reconstruction. If an electrocatalyst does not undergo reconstruction to activate the OER, studies on the active site configurations should be much easier, and the resolved data would be more accurate. In addition, molar concentrations of OH^- are temperature-dependent.[54] A more precise calculation of the rate constant for benchmarking E_a values may require OH^- activities (a_{OH}) to be realized, although in this work the difference in a_{OH} between 30 to 60 °C is insignificant (ca. ∼0.0005) in 1 M KOH.[54] A systematic investigation on the complex oxide systems would be worthwhile to acquire a more comprehensive understanding of using high numbers of dopants to lower the activation energy barriers in the OER.

In summary, we have demonstrated that the activation energy is an effective index to evaluate the overall performance of complex oxide electrocatalysts and is potentially useful to quantitatively judge the reactivity of intermediate phases of site reconstruction. We found that, with a higher number of dopant species, fewer degrees of site reconstruction are likely to happen in our ARD-based samples. Reconstruction may not be necessarily be potential dependent and also may not be absolutely required to reach a high-performance OER. These discoveries may provide useful guidelines for the future designs of complex oxide electrocatalysts.

https://doi.org/10.1021/acsenergylett.2c01103
ACS Energy Lett. 2022, 7, 2236−2243

■ ASSOCIATED CONTENT

Supporting Information

The Supporting Information is available free of charge at https://pubs.acs.org/doi/10.1021/acsenergylett.2c01103.

Experimental procedures, TEM images of the catalysts, SEM, the double-layer capacitance (C_{dl}), the order of the reaction of all the catalysts, and additional figures and tables (PDF)

■ AUTHOR INFORMATION

Corresponding Author

Chun-Hu Chen − *Department of Chemistry, National Sun Yat-sen University, Kaohsiung 80424, Taiwan;* orcid.org/0000-0002-3512-6880; Email: chunhu.chen@mail.nsysu.edu.tw

Authors

Tilahun Awoke Zegeye − *Department of Chemistry, National Sun Yat-sen University, Kaohsiung 80424, Taiwan;* orcid.org/0000-0001-8920-8729

Wen-Tai Chen − *Department of Chemistry, National Sun Yat-sen University, Kaohsiung 80424, Taiwan*

Chun-Cheng Hsu − *Department of Chemistry, National Sun Yat-sen University, Kaohsiung 80424, Taiwan*

Joey Andrew A. Valinton − *Department of Chemistry, National Sun Yat-sen University, Kaohsiung 80424, Taiwan;* orcid.org/0000-0002-5244-3765

Complete contact information is available at: https://pubs.acs.org/10.1021/acsenergylett.2c01103

Author Contributions

The manuscript was written through contributions of all authors. All authors have given approval to the final version of the manuscript.

Notes

The authors declare no competing financial interest.

■ ACKNOWLEDGMENTS

The authors acknowledge financial support from the Ministry of Science and Technology, Taiwan, under grants MOST 110-2811-M-110-505, 110-2811-M-110-509, and 109-2628-M-110-001-MY3.

■ REFERENCES

(1) Gao, L.; Cui, X.; Sewell, C. D.; Li, J.; Lin, Z. Recent advances in activating surface reconstruction for the high-efficiency oxygen evolution reaction. *Chem. Soc. Rev.* **2021**, *50* (15), 8428−8469.

(2) Fabbri, E.; Nachtegaal, M.; Binninger, T.; Cheng, X.; Kim, B.-J.; Durst, J.; Bozza, F.; Graule, T.; Schäublin, R.; Wiles, L.; Pertoso, M.; Danilovic, N.; Ayers, K. E.; Schmidt, T. J. Dynamic surface self-reconstruction is the key of highly active perovskite nano-electrocatalysts for water splitting. *Nat. Mater.* **2017**, *16* (9), 925−931.

(3) Zhai, L.; Benedict Lo, T. W.; Xu, Z.-L.; Potter, J.; Mo, J.; Guo, X.; Tang, C. C.; Edman Tsang, S. C.; Lau, S. P. In Situ Phase Transformation on Nickel-Based Selenides for Enhanced Hydrogen Evolution Reaction in Alkaline Medium. *ACS Energy Lett.* **2020**, *5* (8), 2483−2491.

(4) Solomon, G.; Landström, A.; Mazzaro, R.; Jugovac, M.; Moras, P.; Cattaruzza, E.; Morandi, V.; Concina, I.; Vomiero, A. NiMoO4@Co_3O_4 Core−Shell Nanorods: In Situ Catalyst Reconstruction toward High Efficiency Oxygen Evolution Reaction. *Adv. Energy Mater.* **2021**, *11* (32), 2101324−2101337.

(5) Wu, T.; Sun, S.; Song, J.; Xi, S.; Du, Y.; Chen, B.; Sasangka, W. A.; Liao, H.; Gan, C. L.; Scherer, G. G.; Zeng, L.; Wang, H.; Li, H.; Grimaud, A.; Xu, Z. J. Iron-facilitated dynamic active-site generation on spinel CoAl2O4 with self-termination of surface reconstruction for water oxidation. *Nat. Catal.* **2019**, *2* (9), 763−772.

(6) Sun, H.; Xu, X.; Song, Y.; Zhou, W.; Shao, Z. Designing High-Valence Metal Sites for Electrochemical Water Splitting. *Adv. Funct. Mater.* **2021**, *31* (16), 2009779−2009822.

(7) Burke, M. S.; Kast, M. G.; Trotochaud, L.; Smith, A. M.; Boettcher, S. W. Cobalt−Iron (Oxy)hydroxide Oxygen Evolution Electrocatalysts: The Role of Structure and Composition on Activity, Stability, and Mechanism. *J. Am. Chem. Soc.* **2015**, *137* (10), 3638−3648.

(8) Moysiadou, A.; Lee, S.; Hsu, C.-S.; Chen, H. M.; Hu, X. Mechanism of Oxygen Evolution Catalyzed by Cobalt Oxyhydroxide: Cobalt Superoxide Species as a Key Intermediate and Dioxygen Release as a Rate-Determining Step. *J. Am. Chem. Soc.* **2020**, *142* (27), 11901−11914.

(9) Görlin, M.; Halldin Stenlid, J.; Koroidov, S.; Wang, H.-Y.; Börner, M.; Shipilin, M.; Kalinko, A.; Murzin, V.; Safonova, O. V.; Nachtegaal, M.; Uheida, A.; Dutta, J.; Bauer, M.; Nilsson, A.; Diaz-Morales, O. Key activity descriptors of nickel-iron oxygen evolution electrocatalysts in the presence of alkali metal cations. *Nat. Commun.* **2020**, *11* (1), 6181−6191.

(10) Liao, P.-C.; Jhang, R.-H.; Chiu, Y.-H.; Valinton, J. A. A.; Yeh, C.-H.; Ebajo, V. D.; Wang, C.-H.; Chen, C.-H. Rock Salt Oxide Hollow Spheres Achieving Durable Performance in Bifunctional Oxygen Energy Cells. *ACS Appl. Energy Mater.* **2021**, *4* (4), 3448−3459.

(11) Kim, B.-J.; Cheng, X.; Abbott, D. F.; Fabbri, E.; Bozza, F.; Graule, T.; Castelli, I. E.; Wiles, L.; Danilovic, N.; Ayers, K. E.; Marzari, N.; Schmidt, T. J. Highly Active Nanoperovskite Catalysts for Oxygen Evolution Reaction: Insights into Activity and Stability of Ba0.5Sr0.5-Co0.8Fe0.2O2+δ and PrBaCo2O5+δ. *Adv. Funct. Mater.* **2018**, *28* (45), 1804355−1804366.

(12) Zhu, Y.; Wang, J.; Chu, H.; Chu, Y.-C.; Chen, H. M. In Situ/Operando Studies for Designing Next-Generation Electrocatalysts. *ACS Energy Lett.* **2020**, *5* (4), 1281−1291.

(13) Shih, M.-C.; Jhang, R.-H.; Tsai, Y.-T.; Huang, C.-W.; Hung, Y.-J.; Liao, M.-Y.; Huang, J.; Chen, C.-H. Discontinuity-Enhanced Thin Film Electrocatalytic Oxygen Evolution. *Small* **2019**, *15* (50), 1903363−1903371.

(14) Zhang, L.; Jang, H.; Liu, H.; Kim, M. G.; Yang, D.; Liu, S.; Liu, X.; Cho, J. Sodium-Decorated Amorphous/Crystalline RuO_2 with Rich Oxygen Vacancies: A Robust pH-Universal Oxygen Evolution Electrocatalyst. *Angew. Chem., Int. Ed.* **2021**, *60* (34), 18821−18829.

(15) Swierk, J. R.; Klaus, S.; Trotochaud, L.; Bell, A. T.; Tilley, T. D. Electrochemical Study of the Energetics of the Oxygen Evolution Reaction at Nickel Iron (Oxy)Hydroxide Catalysts. *J. Phys. Chem. C* **2015**, *119* (33), 19022−19029.

(16) Yeh, C.-H.; Hsu, W.-Y.; Hsu, C.-C.; Valinton, J. A. A.; Yang, C.-I.; Chiu, C.-c.; Chen, C.-H. Cobalt Iron Oxides Prepared by Acidic Redox-Assisted Precipitation: Characterization, Applications, and New Opportunities. *ACS Appl. Mater. Interfaces* **2021**, *13* (44), 52181−52192.

(17) Zhu, Y.; Tahini, H. A.; Hu, Z.; Chen, Z.-G.; Zhou, W.; Komarek, A. C.; Lin, Q.; Lin, H.-J.; Chen, C.-T.; Zhong, Y.; Fernández-Díaz, M. T.; Smith, S. C.; Wang, H.; Liu, M.; Shao, Z. Boosting Oxygen Evolution Reaction by Creating Both Metal Ion and Lattice-Oxygen Active Sites in a Complex Oxide. *Adv. Mater.* **2020**, *32* (1), 1905025−1905032.

(18) Zhang, N.; Feng, X.; Rao, D.; Deng, X.; Cai, L.; Qiu, B.; Long, R.; Xiong, Y.; Lu, Y.; Chai, Y. Lattice oxygen activation enabled by high-valence metal sites for enhanced water oxidation. *Nat. Commun.* **2020**, *11* (1), 4066−4076.

(19) Jhang, R.-H.; Yang, C.-Y.; Shih, M.-C.; Ho, J.-Q.; Tsai, Y.-T.; Chen, C.-H. Redox-assisted multicomponent deposition of ultrathin amorphous metal oxides on arbitrary substrates: highly durable cobalt manganese oxyhydroxide for efficient oxygen evolution. *J. Mater. Chem. A* **2018**, *6* (37), 17915−17928.

(20) Kuo, C.-C.; Lan, W.-J.; Chen, C.-H. Redox preparation of mixed-valence cobalt manganese oxide nanostructured materials: highly efficient noble metal-free electrocatalysts for sensing hydrogen peroxide. *Nanoscale* **2014**, *6* (1), 334−341.
(21) Chen, C.-H.; Abbas, S. F.; Morey, A.; Sithambaram, S.; Xu, L.-P.; Garces, H. F.; Hines, W. A.; Suib, S. L. Controlled Synthesis of Self-Assembled Metal Oxide Hollow Spheres Via Tuning Redox Potentials: Versatile Nanostructured Cobalt Oxides. *Adv. Mater.* **2008**, *20* (6), 1205−1209.
(22) Montini, T.; Melchionna, M.; Monai, M.; Fornasiero, P. Fundamentals and Catalytic Applications of CeO_2-Based Materials. *Chem. Rev.* **2016**, *116* (10), 5987−6041.
(23) Liang, F.; Yu, Y.; Zhou, W.; Xu, X.; Zhu, Z. Highly defective CeO_2 as a promoter for efficient and stable water oxidation. *J. Mater. Chem. A* **2015**, *3* (2), 634−640.
(24) Abdel Ghany, N.; Meguro, S.; Kumagai, N.; Asami, K.; Hashimoto, K. Anodically Deposited Mn-Mo-Fe Oxide Anodes for Oxygen Evolution in Hot Seawater Electrolysis. *Mater. Trans.* **2003**, *44*, 2114−2123.
(25) Dong, R.; Du, H.; Sun, Y.; Huang, K.; Li, W.; Geng, B. Selective Reduction−Oxidation Strategy to the Conductivity-Enhancing Ag-Decorated Co-Based 2D Hydroxides as Efficient Electrocatalyst in Oxygen Evolution Reaction. *ACS Sustainable Chem. Eng.* **2018**, *6* (10), 13420−13426.
(26) Zuo, Y.; Liu, Y.; Li, J.; Du, R.; Han, X.; Zhang, T.; Arbiol, J.; Divins, N. J.; Llorca, J.; Guijarro, N.; Sivula, K.; Cabot, A. In Situ Electrochemical Oxidation of Cu_2S into CuO Nanowires as a Durable and Efficient Electrocatalyst for Oxygen Evolution Reaction. *Chem. Mater.* **2019**, *31* (18), 7732−7743.
(27) Snir, N.; Yatom, N.; Caspary Toroker, M. Progress in understanding hematite electrochemistry through computational modeling. *Comput. Mater. Sci.* **2019**, *160*, 411−419.
(28) Bai, L.; Lee, S.; Hu, X. Spectroscopic and Electrokinetic Evidence for a Bifunctional Mechanism of the Oxygen Evolution Reaction. *Angew. Chem., Int. Ed.* **2021**, *60* (6), 3095−3103.
(29) Lyons, M.; Brandon, M. The Oxygen Evolution Reaction on Passive Oxide Covered Transition Metal Electrodes in Aqueous Alkaline Solution. Part1-Nickel. *Int. J. Electrochem. Sci.* **2008**, *3*, 1386−1424.
(30) Yeo, B. S.; Bell, A. T. In Situ Raman Study of Nickel Oxide and Gold-Supported Nickel Oxide Catalysts for the Electrochemical Evolution of Oxygen. *J. Phys. Chem. C* **2012**, *116* (15), 8394−8400.
(31) Dionigi, F.; Strasser, P. NiFe-Based (Oxy) hydroxide Catalysts for Oxygen Evolution Reaction in Non-Acidic Electrolytes. *Adv. Energy Mater.* **2016**, *6* (23), 1600621−1600640.
(32) Suermann, M.; Schmidt, T. J.; Büchi, F. N. Comparing the kinetic activation energy of the oxygen evolution and reduction reactions. *Electrochim. Acta* **2018**, *281*, 466−471.
(33) Zhou, G.; Wang, D. W.; Yin, L. C.; Li, N.; Li, F.; Cheng, H. M. Oxygen bridges between NiO nanosheets and graphene for improvement of lithium storage. *ACS Nano* **2012**, *6* (4), 3214−3223.
(34) Trotochaud, L.; Young, S. L.; Ranney, J. K.; Boettcher, S. W. Nickel-Iron Oxyhydroxide Oxygen-Evolution Electrocatalysts: The Role of Intentional and Incidental Iron Incorporation. *J. Am. Chem. Soc.* **2014**, *136*, 6744−6753.
(35) Klaus, S.; Cai, Y.; Louie, M. W.; Trotochaud, L.; Bell, A. T. Effects of Fe Electrolyte impurities on $Ni(OH)_2$/NiOOH structure and Oxygen Eolution Activity. *J. Phys.Chem.C* **2015**, *119*, 7243−7254.
(36) Lodi, G.; Sivieri, E.; Debattsti, A.; Strasatti, S. Ruthenium dioxide-based film electrodes: Effect of chemical composition and surface morphology on oxygen evolution in acid solutions. *J. Appl. Electrochem.* **1978**, *8*, 135−143.
(37) Ardizzone, S.; Falciola, M.; Trasatti, S. Effect of the Nature of the Precursor on the Electrocatalytic Properties of Thermally Prepared Ruthenium Oxide. *J. Electrochem. Soc.* **1989**, *136*, 1545−1550.
(38) Rao, R. R.; Huang, B.; Katayama, Y.; Hwang, J.; Kawaguchi, T.; Lunger, J. R.; Peng, J.; Zhang, Y.; Morinaga, A.; Zhou, H.; You, H.; Shao-Horn, Y. pH- and Cation-Dependent Water Oxidation on Rutile RuO_2(110). *J. Phys. Chem. C* **2021**, *125*, 8195−8207.
(39) Duan, Y.; Yu, Z.-Y.; Hu, S.-J.; Zheng, X.-S.; Zhang, C.-T.; Ding, H.-H.; Hu, B.-C.; Fu, Q.-Q.; Yu, Z.-L.; Zheng, X.; Zhu, J.-F.; Gao, M.-R.; Yu, S.-H. Scaled-Up Synthesis of Amorphous NiFeMo Oxides and Their Rapid Surface Reconstruction for Superior Oxygen Evolution Catalysis. *Angew. Chem., Int. Ed.* **2019**, *58* (44), 15772−15777.
(40) Da Silva, L.; Vilea Franco, D.; Faria, L.; Boodts, J. Surface, kinetics and electrocatalytic properties of Ti/(IrO_2+Ta_2O_5) electrodes, prepared using controlled cooling rate, for ozone production. *Electrochim. Acta* **2004**, *49*, 3977−3988.
(41) Bard, A. J.; Faulkner, L. R. *Electrochemical Methods: Fundamentals and Applications*, 2nd ed.; Wiley: 2000.
(42) Duan, Y.; Dubouis, N.; Huang, J.; Dalla Corte, D. A.; Pimenta, V.; Xu, Z. J.; Grimaud, A. Revealing the Impact of Electrolyte Composition for Co-Based Water Oxidation Catalysts by the Study of Reaction Kinetics Parameters. *ACS Catal.* **2020**, *10* (7), 4160−4170.
(43) Bockris, J. O. M.; Otagawa, T. Mechanism of oxygen evolution on perovskites. *J. Phys. Chem.* **1983**, *87* (15), 2960−2971.
(44) Lin, F.; Markus, I. M.; Nordlund, D.; Weng, T.-C.; Asta, M. D.; Xin, H. L.; Doeff, M. M. Surface reconstruction and chemical evolution of stoichiometric layered cathode materials for lithium-ion batteries. *Nat. Commun.* **2014**, *5* (1), 3529−3537.
(45) Yang, Y.; Fei, H.; Ruan, G.; Xiang, C.; Tour, J. M. Efficient Electrocatalytic Oxygen Evolution on Amorphous Nickel−Cobalt Binary Oxide Nanoporous Layers. *ACS Nano* **2014**, *8* (9), 9518−9523.
(46) Xin, Y.; Dai, X.; Lv, G.; Wei, X.; Li, S.; Li, Z.; Xue, T.; Shi, M.; Zou, K.; Chen, Y.; Liu, Y. Stability-Enhanced α-Ni(OH)2 Pillared by Metaborate Anions for Pseudocapacitors. *ACS Appl. Mater. Interfaces* **2021**, *13* (24), 28118−28128.
(47) Hall, D. S.; Lockwood, D. J.; Bock, C.; MacDougall, B. R. Nickel hydroxides and related materials: a review of their structures, synthesis and properties. *Proc. R. Soc. A* **2015**, *471* (2174), 20140792−20140856.
(48) Radinger, H.; Connor, P.; Tengeler, S.; Stark, R. W.; Jaegermann, W.; Kaiser, B. Importance of Nickel Oxide Lattice Defects for Efficient Oxygen Evolution Reaction. *Chem. Mater.* **2021**, *33* (21), 8259−8266.
(49) Amutha, R.; Muruganandham, M.; Sathish, M.; Akilandeswari, S.; Suri, R. P. S.; Repo, E.; Sillanpää, M. Crystallization-Induced Top-Down Wormlike Hierarchical Porous α-Fe2O3 Self-Assembly. *J. Phys. Chem. C* **2011**, *115* (14), 6367−6374.
(50) Deshpande, N. G.; Kim, D. S.; Ahn, C. H.; Jung, S. H.; Kim, Y. B.; Lee, H. S.; Cho, H. K. β-like FeOOH Nanoswords Activated by Ni Foam and Encapsulated by rGO toward High Current Densities, Durability, and Efficient Oxygen Evolution. *ACS Appl. Mater. Interfaces* **2021**, *13* (16), 18772−18783.
(51) Louie, M. W.; Bell, A. T. An investigation of thin-film Ni-Fe oxide catalysts for the electrochemical evolution of oxygen. *J. Am. Chem. Soc.* **2013**, *135* (33), 12329−12337.
(52) Zhang, Z.; Mao, M. M.; Wang, J.; Gludovatz, B.; Zhang, Z.; Mao, S. X.; George, E. P.; Yu, Q.; Ritchie, R. O. Nanoscale origins of the damage tolerance of the high-entropy alloy CrMnFeCoNi. *Nat. Commun.* **2015**, *6* (1), 10143−10148.
(53) Liu, L.; Paudel, R.; Liu, Y.; Zhu, J.-C. Theoretical Study on Structural Stability and Elastic Properties of Fe (25) Cr(25)Ni(25)-Ti(x)Al((25-x)) Multi-Principal Element *Alloys. Mater. (Basel, Switzerland)* **2021**, *14* (4), 1040−1061.
(54) Hausmann, J. N.; Traynor, B.; Myers, R. J.; Driess, M.; Menezes, P. W. The pH of Aqueous NaOH/KOH Solutions: A Critical and Non-trivial Parameter for Electrocatalysis. *ACS Energy Lett.* **2021**, *6* (10), 3567−3571.

https://doi.org/10.1021/acsenergylett.2c01103
ACS Energy Lett. 2022, 7, 2236−2243